Hydrodynamics and mass transport in an anodic oxidation reactor: Influence of gas evolution and flow path through mesh electrodes

Màxim Gibert-Vilas, Yoan Pechaud, Abderrahmane Kherbeche, Nihal Oturan, Laurent Gautron, Mehmet A Oturan, Clément Trellu

Chemical Engineering Journal 500 (2024) 157059

Contents lists available at ScienceDirect

Chemical Engineering Journal

journal homepage: www.elsevier.com/locate/cej

Hydrodynamics and mass transport in an anodic oxidation reactor: Influence of gas evolution and flow path through mesh electrodes

Màxim Gibert-Vilas, Yoan Pechaud *, Abderrahmane Kherbeche, Nihal Oturan, Laurent Gautron, Mehmet A. Oturan, Clément Trellu *

Université Gustave Eiffel, Laboratoire Géomatériaux et Environnement, EA 4508, 77454 Marne-la-Vallée, Cedex 2, France

ARTICLE INFO

Keywords:
Anodic oxidation
Hydrodynamics
Mass transport
Modeling
Organic pollutant
Water treatment
Mesh electrodes

ABSTRACT

Removal of organic compounds by anodic oxidation requires a sufficiently high rate of mass transport of target compounds to the electrode surface. Since anodic oxidation is often accelerated by the formation of hydroxyl radicals from water oxidation at high anodic potential, the role of oxygen/hydrogen evolution reactions was investigated. Residence time distributions showed that formation of bubbles in zones where fluid velocity was minimal, allowed for strongly improving global hydrodynamics in the reactor. The role of bubbles was also discussed by comparing mass transport coefficients obtained from the limiting current technique to values obtained from kinetics of COD removal during treatment of a model pollutant (phenol). The use of mesh electrodes (with liquid flowing through the electrode) further promoted convection and mass transport of organic compounds compared to plates. However, large bubbles generated at the surface of the plate electrodes also enhanced convection in their vicinity. In both cases, an adverse effect from bubble adhesion was observed because of the decrease in the active surface of electrodes. The mass transport coefficient obtained with the limiting current technique using mesh electrodes was 0.69×10^{-3} cm s^{-1} at 10.8 L h^{-1} with a mean velocity of electrolyte past the mesh surface ($\overline{u}_{mesh}$) of 0.37 cm s^{-1}. It decreased to 0.58×10^{-3} cm s^{-1} during the treatment of phenol at the same flow rate and reached 0.75×10^{-3} cm s^{-1} when increasing the flow rate to 32.4 L h^{-1}. By taking into consideration gas evolution at the surface of electrodes, this study allowed for accurate calibration of an advective – dispersive model with reaction that could be used for sizing such reactors according to the intended application.

Abbreviations: ***Ae*,** the volumetric surface area (ratio between the geometric volume and the active surface area of the mesh electrodes) (cm^{-1}); **C_A,** aeration by a floor diffuser of fine bubbles and no current at the electrodes; **C_{EP},** polarization of the electrodes with a current intensity and no aeration; **C_W,** no electrode polarization and no aeration; **COD,** chemical oxygen demand (mgO_2 L^{-1}); ***D_i*,** diffusion coefficient of specie i (m^2 s^{-1}); ***D*,** dispersion coefficient (cm^2 min^{-1}); **E(θ),** residence time distribution function; **EC,** electrical energy consumption (kWh $gCOD^{-1}$); ***F*,** Faraday constant (96485 C mol^{-1}); **HER,** hydrogen evolution reaction; **IOA,** index of agreement; ***k_m*,** mass transport coefficient (m s^{-1}); **MCE,** mineralization current efficiency; **ME,** model efficiency; **OER,** oxygen evolution reaction; **$^{\bullet}$OH,** hydroxyl radical; ***Q_l*,** liquid flow rate (L h^{-1}); ***rAO*:** anodic oxidation rate (mol m^{-3} s^{-1}); **RTD:** residence time distribution; **$\overline{t_s}$:** mean residence time or first moment order; **$\overline{u}$:** mean flow velocity (m s^{-1}); ***V_T*:** total volume (L); **σ^2:** variance or second moment order; **γ:** skewness factor or third moment order; **τ:** residence time; **μ:** order moment.

1. Introduction

Electrochemical flow cells are used for various applications including chlor-alkali industry [1], H_2O_2 synthesis [2], CO_2 reduction [3,4], electrochemically mediated carbon capture [5] or NH_3 production [6]. They are also developed for electrochemical advanced oxidation processes applied in water and wastewater treatment for the removal of organic contaminants [7–12]. Particularly, anodic oxidation allows for non-selective removal of organic compounds due to the production of $^{\bullet}$OH that are obtained from water oxidation at the surface of suitable anode materials such as boron-doped diamond (BDD) [13,14]. These oxidant species ($E^{\circ}(^{\bullet}OH/H_2O) = 2{,}8$ V/NHE) are able to react quickly

* Corresponding authors.

https://doi.org/10.1016/j.cej.2024.157059
Received 23 July 2024; Received in revised form 18 October 2024; Accepted 22 October 2024
Available online 24 October 2024

and non-selectively with a large range of organic pollutants. These reactions lead to either the formation of intermediates or full mineralization to CO_2, H_2O and inorganic ions, depending on the operating conditions [12,15]. Other oxidant species (e.g., active chlorine, sulfate radicals) may also be produced depending on both nature of the electrode material and presence of inorganic ions in the effluent [7].

Three main types of undivided electrochemical cells are reported for such application. Small stirred-tank reactors operated in batch conditions are typically used for testing new electrode materials at lab-scale [16–21]. The design of suitable flow cells is then a key step for further development and scale-up of electrochemical processes for water and wastewater treatment [12,22–30]. Flow-by cells or filter press cells allow for a better control of mass transport conditions [31–36], which is a key issue for scaling-up electrochemical reactors [37]. Flow-through cells based on porous electrodes improve mass transport conditions because of larger electro-active surface area and faster diffusion of target pollutants within small electrode pores. This latter configuration is particularly convenient for the treatment of low concentrations of target pollutants [38,39].

Process effectiveness for removal of organic pollutants strongly depends on reactions occurring in the vicinity of the electrode material since most of oxidant species that are electrochemically generated have a very short lifetime, particularly $^{\bullet}OH$ ($\approx 10^{-8}$ s) [40,41]. Therefore, hydrodynamics and mass transport rates from the bulk to the electrode surface are crucial parameters to take into consideration for process optimization. Besides, anodic oxidation process requires the use of high anodic potential for generation of $^{\bullet}OH$. Thus, this process is necessarily operated in the potential region of water oxidation and large amounts of gas bubbles are generated at the surface of electrodes from oxygen and hydrogen evolution reactions (OER / HER).

In a previous study, a flow reactor was developed using 14 plate anodes and 14 plate cathodes, arranged in parallel to form a serpentine reactor with a horizontal flow between electrodes [29]. Such reactor design is comparable to several flow-by cells placed in series. The main advantages of such configuration are (i) the ability to treat concentrated effluents with high content of particulate matter because of low fouling issues, (ii) avoiding the accumulation of bubbles from gas evolution due to the open configuration of the reactor, (iii) the possibility to easily modulate the interelectrode gap, as well as the number and type of electrodes.

In the present study, this configuration was compared with a new one based on the use of 14 mesh anodes and 14 mesh cathodes with the liquid flowing through the mesh structure in order to improve mass transport conditions. A novel approach was developed in order to assess and compare the impact of OER / HER (and subsequent growth and transport of gas bubbles) on hydrodynamics and mass transport rates. The impact on process effectiveness for removal of organic compounds was then investigated based on mineralization kinetics of a model compound (phenol). The dissociation of the different phenomena allowed for the development of a modeling approach based on hydrodynamics, local mass transport conditions and reactivity of the electrode with more precise calibration of model parameters. This model allows for prediction of process effectiveness in continuous mode.

2. Material and methods

2.1. Chemicals and analytical methods

The list of chemicals is provided in **Text SM 1**. Details of TOC and COD analyses are provided in **Text SM 2**.

2.2. Anodic oxidation flow reactor

A modular anodic oxidation flow reactor was used for all experiments [29]. It was composed of 28 electrodes set in parallel. 14 anodes and 14 cathodes were placed alternately in the reactor, precisely aligned, with a constant inter-electrode gap of 1.8 cm. The aim was to ensure a constant ohmic drop in order to obtain constant current density / anodic potential distribution along each electrode and from one electrode to another. Total cell voltage was approximately 5.5 V at 4 A and 4.5 V at 1.5 A. This interelectrode distance might be reduced for treating effluent with low conductivity to avoid high ohmic drop. In the present study, two different configurations were compared based on the use of plate or mesh electrodes, as presented in Fig. 1. Plate and mesh anodes were made of a thin film of boron-doped diamond (BDD) deposited onto a niobium (Nb) substrate (Diachem® electrodes from Condias, Germany). The dimensions of plate anodes were 5 × 6 cm. Plate and mesh cathodes were made of stainless steel from Goodfellow (United Kingdom) and Negofiltres (France), respectively. The size of mesh anodes was 6 × 6 cm. The shape of mesh electrodes is described using the dimensions indicated in **Figure SM 1**. The nominal short way, the long way, the width and the gauge were 4, 6, 1 and 1 mm, respectively. In terms of surface area, the percentage of void ascribed to shape of the holes was estimated to be 20 %. The ratio between the active surface area and the geometric volume of the mesh electrodes (*Ae*) was estimated to be 15.9 cm^{-1}.

For the configuration with plate electrodes, the liquid flowed parallel to the surface of electrodes, following a serpentine array. For the configuration with mesh electrodes, the liquid flowed through the mesh structure of electrodes.

The total volume of the reactor was around 1.75 L. The flow rate and operating conditions generated only little variations of reactor volume (water level) (**Table SM 1**). The geometric surface of plate and mesh anodes immerged in water closely matched each other for all experiments (**Table SM 2**). The total geometrical surface area of electrodes was around 624 and 644 cm^2 for plate and mesh electrodes, respectively. Moreover, similar deposition technique (chemical vapor deposition) was used on the two anode types, resulting in similar surface roughness. The reactor was built with a fine bubble diffuser floor that can be used for aeration of the reactor, as previously described [29]. The objective is to provide a reactor that features a modular, compact design with multiple electrode pairs, optimized for mass transport and hydrodynamics, and without clogging issues when treating effluents containing particles.

2.3. Determination of residence time distribution (RTD)

$NaClO_4$ (14.8 mM) was selected as an inert tracer for application in the modular anodic oxidation flow reactor because of absence of oxidation / reduction of ClO_4^- in the range of applied operating conditions. RTD was performed (i) without neither aeration nor electrode polarization (configuration noted as C_W), (ii) with aeration at 0.2 L min^{-1} by the fine bubble diffuser floor but without current supply (noted as C_A), and (iii) with electrode polarization but without aeration (C_{EP}). The solution conductivity was continuously measured at the reactor's outlet by a conductivity meter. Each experiment was performed in triplicate. The term "polarization" refers to the process in which current is applied to the electrode by an external power source. Results of RTD experiments might be extrapolated to other composition of aqueous solutions if fluid properties (e.g. viscosity) are not significantly different.

The distribution function E(t) and the normalized function E(θ) as well as the first, second and third order moments (μ_1, μ_2 and μ_3) equations are presented in **Text SM 3.**

2.4. Determination of local mass transport conditions at electrode surface

Mass transport of a target compound from the bulk to the anode surface was evaluated by determining the mass transport coefficient (noted k_m) according to reactor configuration and flow rate. The coefficient was determined from the limiting current method in a solution containing 100 mM $NaClO_4$, 5 mM $[Fe(CN)_6]^{4-}$ and 20 mM $[Fe(CN)_6]^{3-}$

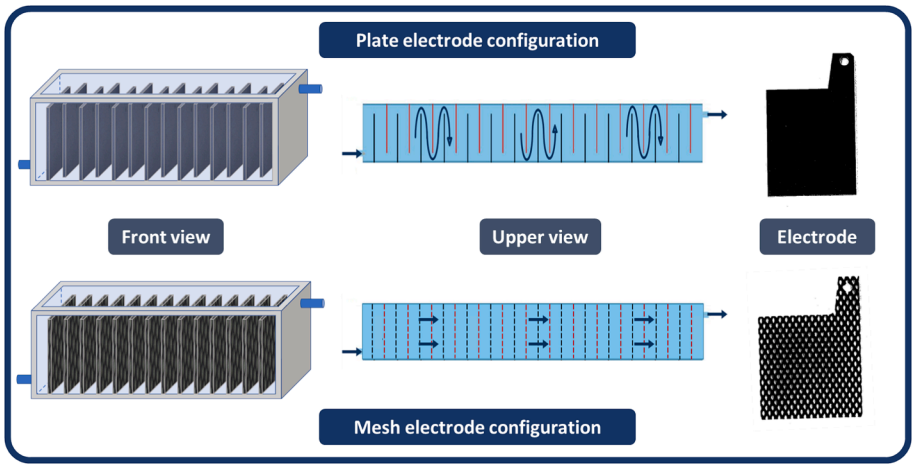

Fig. 1. Schematic view of the two configurations of the modular anodic oxidation flow reactor with plate electrodes or mesh electrodes.

[18,42]. $NaClO_4$ was chosen because it is considered an inert electrolyte, meaning that it represents the final oxidation stage of chlorine, and no reduction is expected under the working conditions. An Ag/AgCl (3 M KCl) reference electrode was added between two electrodes in the middle of the reactor. The limiting current (I_{lim}) for oxidation of $[Fe(CN)_6]^{4-}$ to $[Fe(CN)_6]^{3-}$ was obtained through cyclic voltammetry (10 mV s^{-1}) in the potential range of water stability. The operational conditions were selected based on previous works from Guo et al. (2016) who observed that using higher scan rate (100 mV s^{-1}) led to significant contribution of the charging current to the total current [38]. In the data presented in this article, the charging current might still have a slight impact on the measured limited currents, but only significantly for the lowest values (at low flow rates).

The value of the mass transport coefficient was then obtained using **Equation (1)**.

$$k_m = \frac{I_{lim}}{n\ F\ A\ C} \quad (1)$$

with A the geometric surface of the two sides of the working electrode (m^2), I_{lim} the measured limiting current (A), k_m the mass-transport coefficient (m s^{-1}), C the concentration of $[Fe(CN)_6]^{4-}$ concentration (mol m^{-3}), F the Faraday constant (96485 sA mol^{-1}), and n the number of exchanged electrons during the target reaction (1 electron).

It is important to notice that values of k_m were normalized considering the geometric surface of electrodes. As mentioned before, these values were similar for both plate and mesh anodes.

The limiting current density for an electrochemical reaction (j_{lim}) can be defined thanks to **Equation (2)**.

$$j_{lim} = \frac{I_{lim}}{S} \quad (2)$$

with S the geometric surface of the working electrode (cm^2).

2.5. Experiments on mineralization of a model compound

Phenol was used as a model organic compound for assessment of process effectiveness. Phenol was selected as model pollutant due to (i) the extensive literature in the frame of electrochemical advanced oxidation processes using non-active electrodes, (ii) its ease of implementation at different concentrations, and (iii) its aromatic structure that is common among many micropollutants. The phenol oxidation by hydroxyl radicals into the primary by-products is described in **Text SM 4**.

Different experiments were performed with phenol concentrations in the range 0.01–0.60 g L^{-1}. $NaNO_3$ and Na_2SO_4 were compared, as the first one is considered inert (with no conversion into oxidizing species), while the latter may lead to the formation of other oxidizing species. To ensure a valid comparison of the two systems, the same concentrations (50 mM) were used, resulting in close conductivity of both solutions (around 13 mS cm^{-1}). Experiments were performed with both reactor configurations in either continuous (single pass, 0 % recirculation) or batch (100 % recirculation) mode.

In continuous mode, samples were taken at the reactor outlet after reaching steady state (i.e. after more than three times the hydraulic residence time). Mineralization of phenol was followed through measurements of TOC and COD. Experiments were performed with a flow rate of 10.8 L h^{-1} or 32.4 L h^{-1} and a current intensity of 4 A (corresponding current densities, in the range 6.0 to 6.5 mA cm^{-2} according to reactor configuration, are presented in **Table SM 3**). In recirculation mode, the liquid from the outlet of the reactor was sent to a 0.5 L stirred tank, acting as a buffer tank for recirculation of the liquid towards the inlet of the reactor. Samples were taken at outlet of this tank.

2.6. Modelling approach

An advective – dispersive model with reaction was used to predict the effectiveness of the process according to operating conditions. The model was based on COD removal rate. The following **Equation (3)** was solved numerically by using parameters previously determined by experimental methods:

$$\frac{\partial C}{\partial t} = D\frac{\partial^2 C}{\partial x^2} - \overline{u}\frac{\partial C}{\partial x} - r_{AO} \quad (3)$$

where C is the COD concentration ($gO_2\ m^{-3}$), D is the dispersion coefficient obtained from calibration of the model with experimental RTD curves ($m^2\ s^{-1}$), $\overline{u}$ is the mean flow velocity (m s^{-1}) and r_{AO} is the reaction rate ($gO_2\ m^{-3}\ s^{-1}$).

Depending on the regime, r_{AO} was expressed as follows [29]:

- under mass transport limitation: $r_{AO} = k_m\ a\ C$
- under current limitation: $r_{AO} = \frac{I}{4\ F\ V}$

where k_m is the mass transport coefficient (m s^{-1}) obtained from the calibration of the model with experimental data of COD removal, a is the specific surface of electrodes by reactor volume ($a = A/V$) ($m^2\ m^{-3}$), F is the Faraday constant (96485 C mol^{-1}) and I is the current intensity (A). The computational time for each simulation was in the range of 2–60 s with a classical computer configuration (e.g. processor speed of 1.6 GHZ and 8 GB RAM).

Details of calculations allowing to determine model accuracy are given in **Text SM 5**.

2.7. Parameters to evaluate process efficiency

Electrical energy consumption (EC) (kWh $gCOD^{-1}$) and mineralization current efficiency (MCE) (%) were calculated for assessment of process efficiency. Details of calculations are given in **Text SM 6**.

2.8. Camera experiment and image processing

Bubbles electrochemically generated at electrode surface and gas phase hydrodynamics near electrodes were observed using a color camera (Basler acA1920 – 15Ouc, Germany, 8 bits, 144 Hz, 1344 × 1024 $pixels^2$) placed in front of the 7th compartment region of the reactor. Further details on camera parameters and image processing are given in **Text SM 7**.

3. Results and discussion

3.1. Hydrodynamics

3.1.1. Impact of operating conditions (liquid flow rate, external aeration, current intensity) on RTD curves with plate electrodes

Impact of flow rate on RTD was assessed for the configuration with plate electrodes in three different operating conditions, including (i) without neither aeration nor electrode polarization (configuration noted as C_W), (ii) with aeration at 0.2 L min^{-1} by the fine bubble diffuser floor but without current supply (noted as C_A), and (iii) with electrode polarization in galvanostatic mode but without aeration (C_{EP}) (Fig. 2). RTD curves are usually described as parabolic curves with possible shape discrepancies depending on reactor characteristics and operating conditions. The shape of the RTD curves is thus provide insights into the hydrodynamics of the reactor. Particularly, it allows for identification of recirculations, dead zones or short-circuits.

First, impact of the liquid flow rate on RTD curves was assessed in C_w condition. At high values of θ (typically between 2 and 6), a significant drag on the values of E(θ) was observed (Fig. 2a). It indicated significant recirculations or diffusive dead zones in the reactor. The existence of recirculations within the reactor was further confirmed by the analysis of moments of RTD curves (Fig. 3). For all values of liquid flow rate (i.e., all values of τ), the experimental mean residence time ($\mu_1 = \overline{t_s}$) was always higher than τ (Fig. 3a).

However, a less significant drag phase was observed when increasing the liquid flow rate from 10.8 L h^{-1} to 60 L h^{-1} (Fig. 2a). Furthermore, the higher the liquid flow rate (i.e, the lower the τ), the smaller the difference between τ and experimental mean residence time ($\mu_1 = \overline{t_s}$). These results indicated that using higher flow rate reduced recirculation phenomena occurring within the reactor. These trends are also consistent with evolution of the second order moment ($\mu_2 = \sigma^2$). These values significantly decreased when increasing liquid flow rate, meaning that

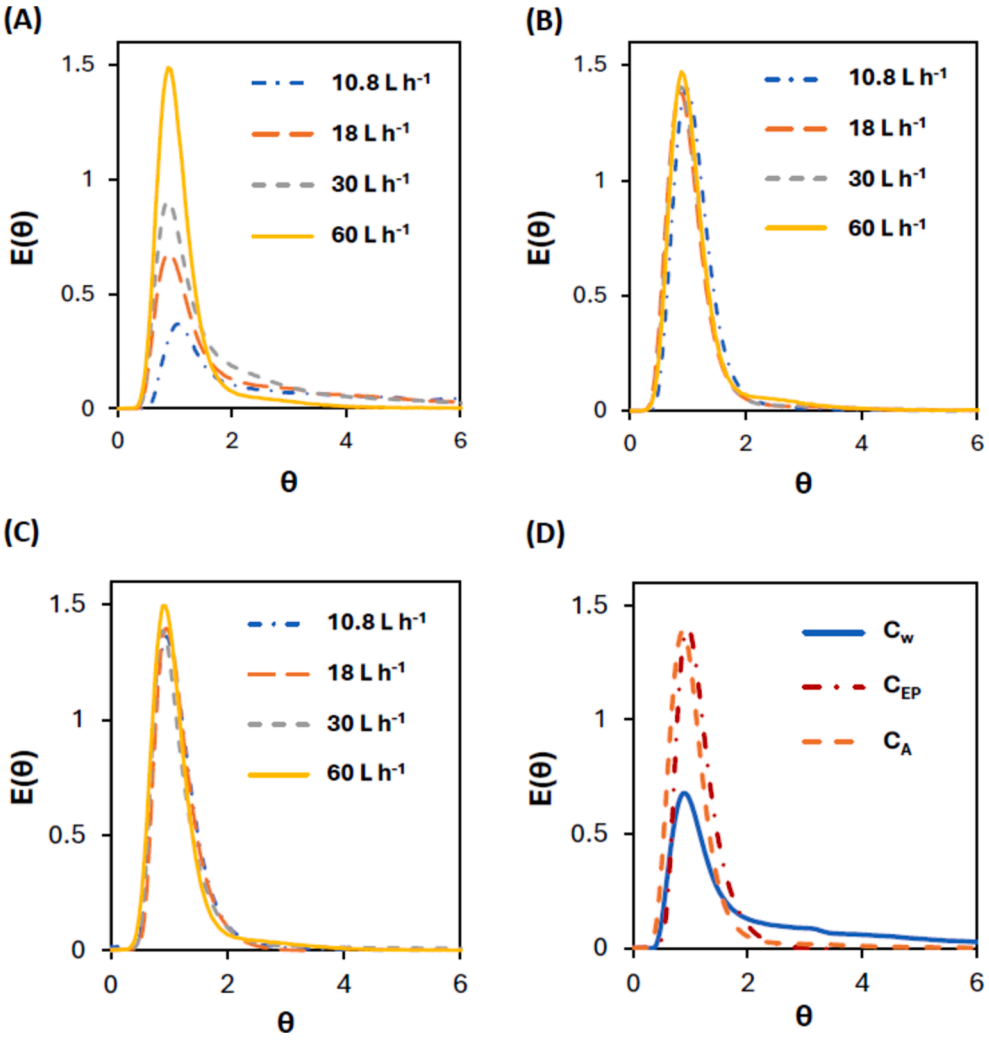

Fig. 2. RTD curves obtained for different conditions and different flow rates: (A) without current and aeration (C_W) at different flow rates, (B) with aeration at 0.2 L min^{-1} and without current (C_A) at different flow rates, (C) with an applied current intensity of 1.5 A and without aeration (C_{EP}) at different flow rates and (D) comparison of the three conditions for a given flow rate of 18 L h^{-1} for the three conditions C_W (——), C_A (— —), and C_{EP} (— •).

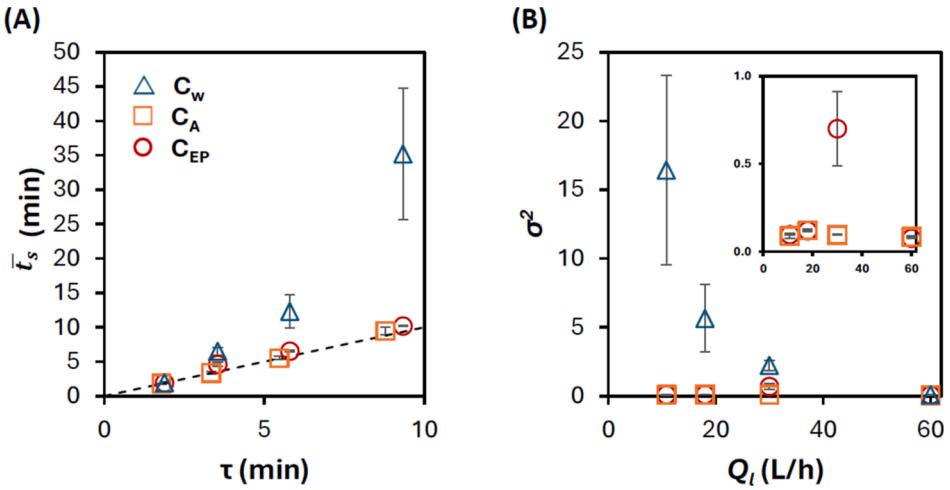

Fig. 3. (A) Experimental mean residence time ($\mu_1 = \overline{t_s}$) as a function of τ values for conditions C_W (△), C_A (□), and C_{EP} (○); the curve for $\overline{t_s} = \tau$ is represented with black dotted line (– – –). (B) Second order moment ($\mu_2 = \sigma^2$) as a function of liquid flow rate (Q_l) for conditions C_W (△), C_A (□), and C_{EP} (○).

the dispersion of E(θ) around the mean value was less important (Fig. 3b).

These results were then compared with the behavior of the reactor for the condition with aeration at 0.2 L min^{-1} by the fine bubble diffuser floor but without current supply (noted as C_A). In this condition, the impact of flow rate on hydrodynamics in the reactor was significantly reduced. All RTD curves had barely the same shape, whatever the liquid flow rate (Fig. 2b). Moreover, non-significant drag phase of E(θ) values was observed and experimental mean residence times ($\mu_1 = \overline{t_s}$) were close to τ (Fig. 3a). In addition, values of the second order moment ($\mu_2 = \sigma^2$) were also relatively constant and low compared to the ones obtained in C_W condition (Fig. 3b). These results emphasized that aeration clearly reduced recirculation phenomena in the reactor, particularly when using low liquid flow rate. These results are in line with a previous study on a similar reactor [29].

A novel objective was then to understand the influence of polarization of electrodes on hydrodynamics in the reactor (condition noted C_{EP}). A current intensity of 1.5 A (corresponding to 2.4 mA cm^{-2}) was applied, resulting in operation of the electrochemical reactor in the potential region required for water splitting. Therefore, OER/HER occurred at anode/cathode and large amounts of O_2 and H_2 bubbles were generated (**Equations (4)** and **(5)**) at the surface of electrodes.

$$2\ H_2O \rightarrow O_2 + 4H^+ + 4\ e^- \quad (4)$$

$$2H^+ + 2\ e^- \rightarrow H_2 \quad (5)$$

Interestingly, global trends of RTD curves were very similar to results obtained with C_A condition, while nonexternal aeration was provided in this condition (Fig. 2c, Fig. 2d and Fig. 4). Similar values of moments were obtained in C_A and C_{EP} conditions (Table 1). It indicated that bubbles from OER / HER influenced RTD in a quite similar way than the aeration by the floor diffusing fine bubbles. For instance, the second order moment ($\mu_2 = \sigma^2$) was 0.12 for both C_A and C_{EP} conditions. It is interesting to notice that gas flow rate within the reactor in condition C_A was much higher than during the condition C_{EP}. Based on Avogadro's law and considering a 100 % Faraday efficiency for OER / HER (**Text SM 8**), the upper limit for O_2 and H_2 gas formation at 1.5 A was only 0.017 L min^{-1} (i.e. more than 11 times lower than the one used for aeration, 0.2 L min^{-1}). Despite this lower gas flow rate, improved hydrodynamics in the reactor in condition C_{EP} might be ascribed to the promotion of micro-turbulences in key zones of the reactor where fluid velocity was low (i.e., near electrodes that were used as reactor walls).

The influence of the value of the current density was then studied by comparing the RTD curves obtained for the same liquid flow rate but different current densities (2.4 *vs* 6.4 mA cm^{-2}, i.e. 1.5 *vs* 4 A) (Fig. 4). The curve obtained at 6.4 mA cm^{-2} presented similar mean residence time ($\mu_1 = \overline{t_s}$) but slightly lower variance ($\mu_2 = \sigma^2 = 0.08$) and skewness factor ($\mu_3 = \gamma = 1.21$) than at 2.4 mA cm^{-2} ($\mu_2 = \sigma^2 = 0.10$ and $\mu_3 = \gamma = 1.60$). These values indicated the presence of few more recirculations or

Table 1
Calculated values of moments of RTD curves obtained at a liquid flow rate of 18 L h^{-1} liquid flow rate for the three different operating conditions (C_W, C_A and C_{EP}).

Parameter	Condition		
	C_W	C_A	C_{EP}
$\mu_1 = \overline{t_s}$ (min)	12.32 ± 2.38	5.52 ± 0.24	6.55 ± 0.10
$\mu_2 = \sigma^2$	5.65 ± 2.47	0.12 ± 0.19	0.12 ± 0.01
$\mu_3 = \gamma$	2.42 ± 1.30	1.27 ± 0.05	1.60 ± 0.22

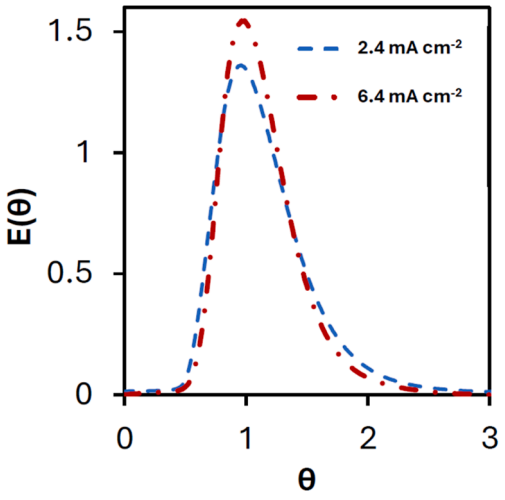

Fig. 4. (A) RTD curves obtained with plate electrodes in the condition C_{EP} with 1.5 A (j_{app} = 2.4 mA cm^{-2}) (—— ——) and 4 A (j_{app} = 6.4 mA cm^{-2}) (—— •) with Q_l = 10.8 L h^{-1}.

diffusive dead zones with an applied current of 2.4 mA cm^{-2}. This trend might be ascribed to the increase in production of bubbles at the electrode surface when using higher current density (the maximum produced gas flow rate was around 0.046 L min^{-1} at 4 A and 0.017 L min^{-1} at 1.5 A (**Text SM 8**)). These bubbles promoted further mixing within the reactor. However, the difference of hydrodynamics was low between these two current densities, thus highlighting that low current density (2.4 mA cm^{-2}) was already sufficient to limit recirculation phenomena.

Overall, these results show that electrode polarization in the potential region of water splitting significantly reduced recirculation phenomena in the reactor, in a similar way than the application of high liquid flow rate (C_W) or external aeration (C_A). Such trend is important to take into consideration since these operating conditions (i.e. high liquid flow rate or aeration) would represent additional operating costs. In addition, from a methodological point of view, the results obtained underlined the importance of considering OER / HER when carrying out RTD experiments for characterization of hydrodynamics in such electrochemical reactor.

3.1.2. Influence of reactor configuration on RTD curves

The influence of reactor configuration (mesh *vs* plate electrodes) was then studied by comparing RTD curves obtained with the same operating conditions. A different behavior was obtained between plate and mesh electrodes for C_W condition (comparison of Fig. 5a and Fig. 2a). However, as for plate electrodes, polarization of mesh electrodes strongly reduced recirculation phenomena (Fig. 5a). Non-significant difference was observed between the two configurations (Fig. 5b), despite the strong difference in terms of liquid circulation inside the reactor. These results indicated that OER / HER was probably the main factor governing the behavior of the reactor in terms of RTD. However, RTD curves are not a sufficient tool for a complete understanding of the specificities related to the two electrodes configurations, particularly when considering local mass transport phenomena at the vicinity of the surface of the electrodes.

3.1.3. RTD curves modelling

A dispersive-diffusive model presented in ***section 2.6*** was used to describe experimental RTD curves obtained with condition C_{EP} (Fig. 6). The key fitting model parameter was the dispersion coefficient (*D*). For both configurations, with a liquid flow rate of 10.8 L h^{-1}, *D* was set at 23.3 mm^2 s^{-1}. ME and IOA parameters were calculated and highlighted a high correlation between model and experimental data for both electrode configurations ($ME_{plate} = 0.968$, $IOA_{plate} = 0.992$; $ME_{mesh} = 0.964$, $IOA_{mesh} = 0.991$).

3.2. Mass transport at the vicinity of the surface of the electrodes

3.2.1. Influence of flow rate on mass transport coefficient using the limiting current method

Mass transport at the local scale of the electrode surface was studied by measurement of mass transport coefficients (k_m) using the limiting current technique for oxidation of $[Fe(CN)_6]^{4-}$. **Figure SM 2** shows a typical current plateau that was obtained. Low scan rate (10 mV s^{-1}) was used as a precaution according to Guo et al. (2016), however, for the lowest liquid flow rates (corresponding to the lowest limiting currents) the charging current may still have contributed in a significant way to the total current [38]. Therefore, obtained k_m values should be considered as an upper bound.

Fig. 7a reveals that increasing the liquid flow rate significantly enhanced mass transport. For instance, for plate electrodes, k_m was 5.0 times higher at 60 L h^{-1} compared to 1.5 L h^{-1}. It was ascribed to the increase in liquid velocity at the vicinity of the surface of the electrodes. Besides, for a given liquid flow rate, k_m was 2 to 3 times higher in the configuration with mesh electrodes compared to plate electrodes (e.g., for $Q_l = 10.8$ L h^{-1}, $k_{m,\ mesh} = 0.69 \times 10^{-3}$ cm s^{-1} and $k_{m,\ plate} = 0.26 \times 10^{-3}$ cm s^{-1}). This difference was directly related to the way the liquid flowed at the vicinity of the electrodes. With mesh electrodes, the liquid flowed through the mesh structure of the electrodes, while the liquid flowed in a parallel way to the surface of plate electrodes. Considering (i) the cross section between two plate electrodes and (ii) the cross section of the reactor minus the solid fraction of mesh electrodes, the liquid mean velocity ($\overline{u}$) was similar for both configurations (e.g., for $Q_l = 10.8$ L h^{-1}, $\overline{u}_{\ mesh} = 3.7$ mm s^{-1} and $\overline{u}_{\ plate} = 3.0$ mm s^{-1}). Therefore, the explanation should be rather ascribed to the strongly different velocity profile at the vicinity of the electrodes surface. The maximum liquid velocity was obtained at the middle of the holes with mesh electrodes (i.e., ≈ 1.5 mm from electrode surface), while the maximum liquid velocity was obtained at the middle of the interelectrode gap (i.e., ≈ 9.3 mm away from electrode surface) with plate electrodes. Therefore, mesh electrodes further improved liquid velocity at the vicinity of surface of electrodes, thus reducing the thickness of the diffusion boundary layer and improving mass transport phenomena from the bulk to the surface of the electrodes.

Mass transport to the surface of electrodes was then further characterized by a correlation between dimensionless numbers, as reported in the literature [42,43]. The theoretical Sherwood number was expressed thanks to Reynolds (*Re*) and Schmidt numbers (*Sc*) according to **Equation** (6).

$$Sh = a\ Re^b\ Sc^{1/3} \tag{6}$$

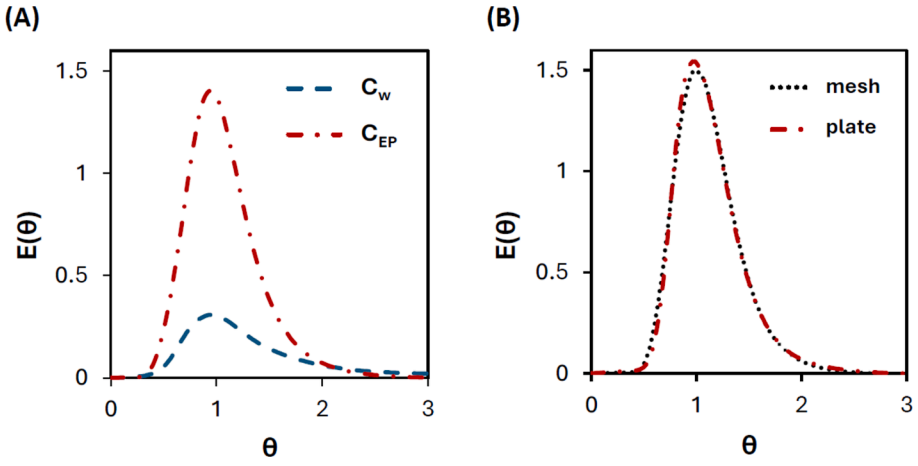

Fig. 5. (A) RTD curves at a liquid flow rate of 18 L h^{-1} using mesh electrodes in condition C_W (— —) and C_{EP} (— •) with $Q_l = 10.8$ L h^{-1} and $I = 4$ A ($j_{app} = 6.4$ mA cm^{-2}). (B) RTD curves obtained in condition C_{EP} with $I = 4$ A ($j_{app} = 6.4$ mA cm^{-2}) and $Q_l = 10.8$ L h^{-1} using plate electrodes (— •) or mesh electrodes (•••••).

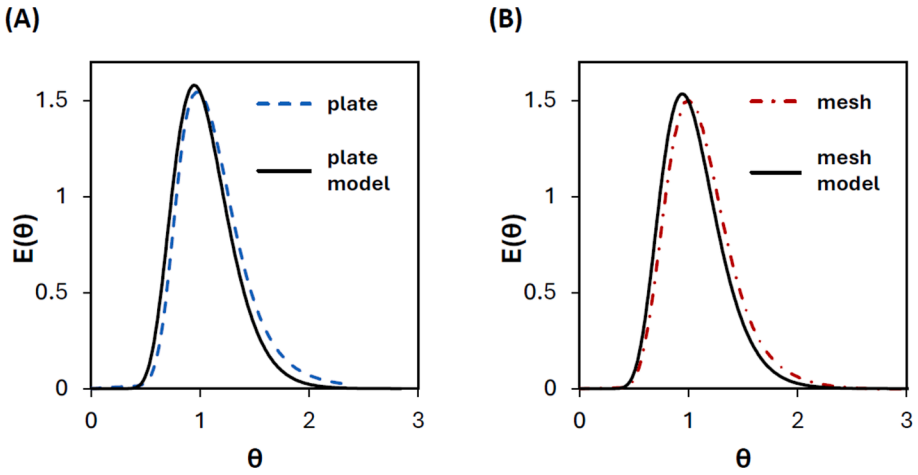

Fig. 6. RTD curves modelling (—) for configurations with (A) plate electrode (— —), and (B) mesh electrode (— •), at a Q_l of 10.8 L h^{-1} in condition C_{EP} with I = 4 A (j_{app} = 6.4 mA cm^{-2}).

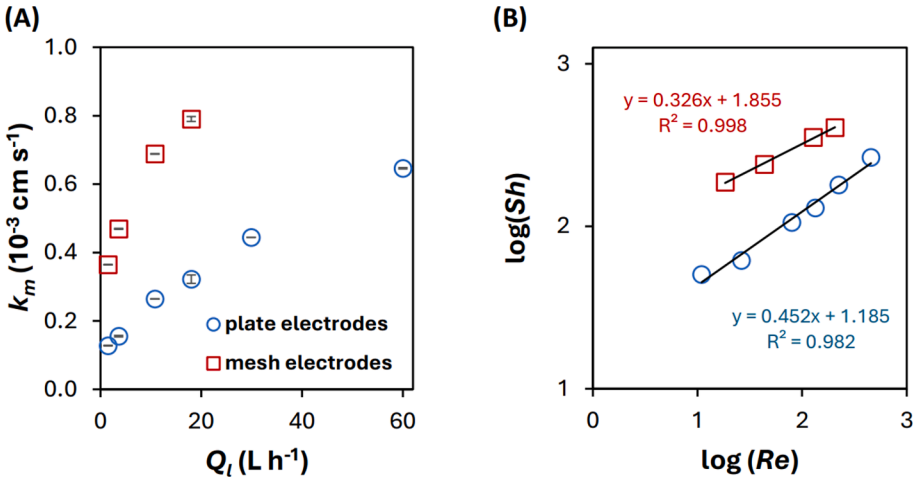

Fig. 7. (A) mass transport coefficient (k_m) as a function of liquid flow rate (Q_l), and (B) log/log plot of Sherwood number (Sh) versus Reynolds number (Re) for the configuration with plate electrodes (○) and mesh electrodes (□).

The values of a and b were obtained from the linear correlation between log(Sh) and log(Re) (**Equation (7)**). Linear correlations obtained for both electrode configurations are shown in Fig. 7b.

$$\log(Sh) = b\,\log(Re) + \log(a) + \tfrac{1}{3}\log(Sc) \tag{7}$$

Sherwood and Reynolds numbers were defined using the equivalent diameter of the flow channel (d_e), which is defined slightly differently in the two electrode configurations due to the different flow paths (**Equations (8)**, **(9)** and **(10)**) [31], and Schmidt number defined according to **Equation (11)**.

$$Sh = \frac{k_m\, d_e}{D_i} \tag{8}$$

$$\mathrm{Re} = \frac{\overline{u}\, d_e}{\nu} \tag{9}$$

$$d_e = \begin{cases} \dfrac{2\, d_{inter}\, h}{d_{inter} + h} & \textit{for plate electrode configuration} \\ \dfrac{2\, l\, h\, \varepsilon}{l + h} & \textit{for mesh electrode configuration} \end{cases} \tag{10}$$

$$Sc = \frac{\nu}{D_i} \tag{11}$$

where k_m is the mass transport coefficient (m s^{-1}), D_i the diffusion coefficient, $\overline{u}$ the liquid mean velocity (m s^{-1}), ν the cinematic viscosity (m^2 s^{-1}), h the height of immerged electrode (m), d_{inter} the interelectrode gap (m), l the length of the electrode and ε the percentage of void within the mesh electrode.

The resulting correlations are presented below for plate electrode configuration (**Equation (12)**), and for mesh electrode configuration (**Equation (13)**):

$$Sh = 1.34\, Re^{0.45}\, Sc^{1/3} \tag{12}$$

$$Sh = 6.24\, Re^{0.33}\, Sc^{1/3} \tag{13}$$

The values of a and b coefficients are related to the design of the reactor. The larger value of a obtained with mesh electrodes highlights the higher relevance of such configuration for enhancing mass transport to the surface of electrodes. Besides, the higher value of b obtained with plate electrodes indicated that the increase in Reynolds number (i.e., higher flow rate) has a greater effect in this case on the increase in mass transport to the surface of electrodes.

3.2.2. Influence of hydrogen and oxygen evolution reactions on mass transport coefficient

It is important to notice that the limiting current technique was based

on measurements performed in the potential region of water stability, meaning that HER and OER did not occur. However, as discussed in the section dedicated to hydrodynamics, gas evolution at the surface of electrodes might strongly influence mass transport conditions.

For a better understanding of the influence of HER and OER on the mass transport coefficient, a different approach was used. The kinetic of COD removal of a model compound (phenol) was monitored using relevant operating conditions: (i) the high current intensity involved that HER and OER occurred and (ii) electro-oxidation of phenol was operated under mass transport limitation with an applied current significantly higher than the limiting current for COD removal. Besides, the kinetic of COD removal was modeled using the advective – dispersive model with reaction described in ***section 2.6***. Using the dispersion coefficient previously obtained, k_m was the only remaining fitting coefficient. Therefore, calibration of the model allowed for determination of another value of k_m that was related to mass transport of phenol from bulk to the surface of electrodes in conditions for which OER and HER occurred. For comparison, values of k_m previously obtained with the limiting current approach were redefined using **Equation (14)** [43].

$$k_{m,phenol} = k_{m,ferrocyanide}\left(\frac{D_{phenol}}{D_{ferrocyanide}}\right)^{2/3} \quad (14)$$

with $D_{ferrocyanide} = 6.62 \times 10^{-10}$ m^2 s^{-1} and $D_{phenol} = 8.83 \times 10^{-10}$ m^2 s^{-1}

Evaluating k_m with this method required the use of an inert electrolyte ($NaNO_3$) to avoid formation of oxidant species that may participate in the oxidation of phenol in the bulk. It is important to notice that the gas production calculations (**Text SM 8**) were conducted under the assumption of a 100 % Faradaic efficiency for gas generation, representing the upper limit. The different configurations were compared at low concentration of a model pollutant (COD = 50 mg O_2 L^{-1}), corresponding to a limiting current of 0.38 A (0.3 mA cm^{-2}), which is significantly lower than the total current of 4 A. Therefore, it can be assumed that the gas evolution efficiency would be high.

When using $NaNO_3$ as supporting electrolyte, 1.8 times faster COD removal was obtained with mesh electrodes compared to plates (Fig. 8a). The kinetic for COD removal experimental data was 0.62 h^{-1} with mesh electrodes and 0.35 h^{-1} with plate electrodes. The difference between the pseudo-first order kinetic constants were in the range of 1 – 5 % when comparing predicted and experimental values. At 10.8 L h^{-1}, for mesh electrodes, the value of k_m calibrated from the model of COD removal was 1.2 times lower than the value obtained with the limiting current approach. On the contrary, for plate electrodes, this value was 1.6 times higher than the value obtained from the limiting current approach (Table 2). Such different trends indicated that another phenomenon might participate in the control of mass transport near the electrode surface. In fact, OER at the anode surface might participate in (i) micro-turbulences near the anode surface during bubble detachment and upward movement, with a positive effect on mass transport of organic compounds to the anode surface, (ii) decreasing the effective active surface area of the electrode because of bubble adhesion, with an adverse effect on mass transport.

In the case of plate electrodes, mass transport was strongly affected by the thick diffusion boundary layer associated to the low liquid velocity near the electrode surface. Therefore, micro-turbulences related to OER might strongly improve mass transport conditions. It might explain the overall increase of k_m value (Table 2) despite the adverse effect of bubble adhesion on active electrode surface.

In the case of mesh electrodes, the liquid velocity profile was more favorable. Therefore, mass transport enhancement from micro-turbulences related to OER was less significant since liquid flow rate might still control convection in the vicinity of the electrode surface. Thus, the decrease of the value of k_m might be ascribed to the adverse effect from bubble adhesion that was in this case the predominant phenomenon. It was further confirmed by results obtained at higher

Table 2
Values of k_m obtained with different methods or operating parameters and using the two different electrodes.

Parameter	Method		
	limiting current method with ferrocyanide* (Q_l = 10.8 L h^{-1})	modelling method with phenol and NO_3^- (Q_l = 10.8 L h^{-1})	modelling method with phenol and NO_3^- (Q_l = 32.4 L h^{-1})
k_m (cm s^{-1}) plate	0.26 × 10^{-3}	0.42 × 10^{-3}	X
k_m (cm s^{-1}) mesh	0.69 × 10^{-3}	0.58 × 10^{-3}	0.75 × 10^{-3}
$km.Ae$ (s^{-1}) mesh	1.10 × 10^{-2}	0.92 × 10^{-2}	1.19 × 10^{-2}

* For comparison, values of k_m obtained with the limiting current method using ferrocyanide have been redefined using **Equation (14)** for phenol molecule.

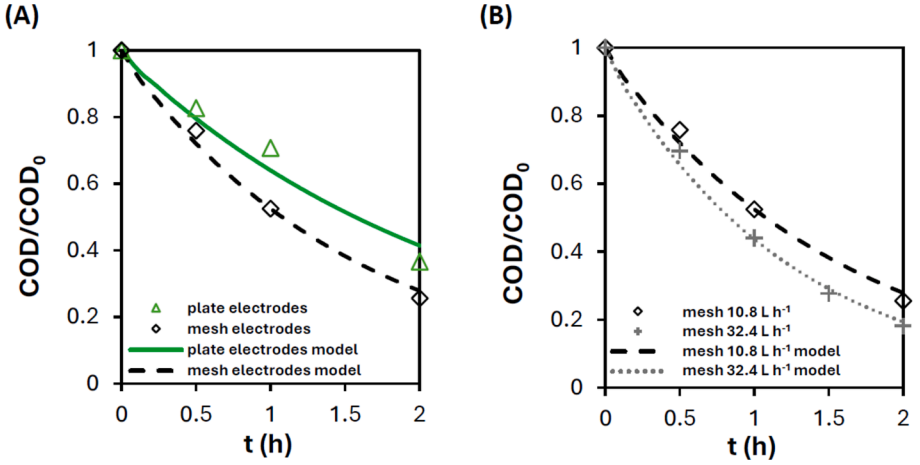

Fig. 8. (A) Evolution of normalized COD (COD/COD$_0$) versus time (h) during treatment of phenol with the following operating conditions: V_T = 2.15 L, Q_l = 10.8 L h^{-1}, [COD]$_0$ = 50 mgO_2 L^{-1} and I = 4 A. Results obtained for plate electrode configuration with $NaNO_3$ electrolyte (△), mesh electrode configuration with $NaNO_3$ electrolyte (◇) and the corresponding curves obtained from the model for plate electrodes (——) (ME = 0.996 and IOA = 0.999), and mesh electrodes (— — —) (ME = 0.999 and IOA = 0.999). (B) Evolution of COD/COD$_0$ versus time (h) during treatment of phenol with the following operating conditions: V_T = 2.15 L, [COD]$_0$ = 50 mgO_2 L^{-1} and I = 4 A. Results obtained for mesh electrode configuration with $NaNO_3$ electrolyte at Q_l = 10.8 L h^{-1} (◇), Q_l = 32.4 L h^{-1} (+) and the corresponding models for Q_l = 10.8 L h^{-1} (— — —) and Q_l = 32.4 L h^{-1} (•••••) (RMSE = 0.999 and IOA = 0.999).

liquid flow rate (Fig. 8b). The increase of liquid flow rate from 10.8 L h^{-1} to 32.4 L h^{-1} with mesh electrodes significantly improved the kinetic for COD removal (from 0.62 h^{-1} to 0.84 h^{-1} for experimental data and from 0.63 to 0.81 for the model), thus resulting in an increase of k_m of 29 % to 0.75 × 10^{-3} cm s^{-1} (Table 2). This k_m value corresponds to a value of *km. Ae* of 1.19 × 10^{-2} s^{-1} (Table 2) which falls within the range reported by Hereijgers et al. (2020) for structured 3D electrodes [30].

Overall, these results indicated that micro-turbulences from OER might have a positive effect on mass transport when experimental conditions (liquid flow rate, electrode configuration) involved low convection in the vicinity of the electrode surface. On the contrary, liquid flow rate might still control mass transport when it provides a sufficiently high liquid velocity in the vicinity of the electrode surface (i.e. at high liquid flow rate and/or with mesh electrodes). Besides, in all cases, bubble adhesion might reduce the active electrode surface. Further investigations would be required for quantification of this adverse effect according to operating conditions.

Bubbles formation and detachment at the anode surface was further studied using optical zoom images (Fig. 9). Pictures revealed that bubbles produced on the anode surface created an upward flow that was similar on both sides of plate anodes, while bubbles were mainly observed at the downstream side of mesh anodes (Fig. 9a and Fig. 9b). The corresponding color map images (Fig. 9c and Fig. 9d) highlighted this trend. Bubbles produced at the upstream side of meshes were swept away by the horizontal liquid flow. These observations confirmed that the upward flow of bubbles might be the controlling phenomenon for convection in the vicinity of plate electrodes, while the horizontal liquid flow through mesh electrodes was controlling convection in the case of meshes.

The upper limit of O_2 gas formation at both sides of one anode was estimated as 1.13 mL min^{-1} (**Text SM 8a**) for both meshes and plates. However, it appeared that bubbles produced at plate electrodes (Fig. 9e) were larger (diameter = 110 μm) and had a much higher velocity (84 mm s^{-1}) than the ones produced at mesh electrodes (diameter = 12 μm, velocity = 6.7 mm s^{-1}) (Fig. 9f). The smaller size of these bubbles may be related to the higher liquid velocity near the electrode surface, which promotes the detachment of small bubbles by providing an additional force to the Archimedes buoyant force for overcoming the adhesion energy. For example, a recent study also reported a strong decrease in size of bubbles that were formed at a Ni mesh when increasing liquid flow rate through the mesh structure [44].

The Reynolds numbers associated to bubble rising (Re_g) defined in **Equation (15)** were 9.2 and 0.08 for plate and mesh electrodes, respectively. Therefore, bubbles generated on plate electrodes may promote further liquid micro-turbulences, thereby enhancing mass transport of pollutants to the electrode surface. This statement might however be modulated by the different number of bubbles produced in the different configurations: smaller frequency of bubbles with a higher Re_g (plate electrodes configuration) and higher frequency of bubbles with a lower Re_g (mesh electrodes configuration).

$$Re_g = \frac{\overline{u}\, r_b}{\nu} \tag{15}$$

With r_b the radius of the bubbles (m), $\overline{u}$ the liquid mean velocity (m s^{-1}), ν the cinematic viscosity (m^2 s^{-1}).

3.3. Application to water treatment with Na_2SO_4 electrolyte

3.3.1. Influence of Na_2SO_4 electrolyte on phenol mineralization

Electrochemically active electrolytes such as Na_2SO_4 are commonly used for assessment of anodic oxidation process effectiveness. In real effluents, presence of diverse ions also leads to generation of oxidant species that can play a key role in COD removal (e.g., active chlorine from Cl^-, sulfate radicals from SO_4^{2-}). The impact of such phenomenon was therefore investigated in this reactor by using Na_2SO_4 instead of $NaNO_3$.

In this case, similar kinetics for COD removal kinetics were obtained with both plate and mesh electrodes (Fig. 10a). It is possible to generate sulfate radicals in presence of sulfate ions based on the following reactions (**Equations (16), (17)** and **(18)**) [7,40,45]. These oxidant species are able to participate in oxidation of organic compounds with a specific feature associated to their longer lifetime compared to hydroxyl radicals (≈ 10^{-5} *vs* 10^{-9} s) [41,46].

$$SO_4^{2-} \rightarrow {}^{\bullet}SO_4^- + e^- \tag{16}$$

$$2\ {}^{\bullet}SO_4^- \rightarrow {}^{\bullet}S_2O_8^{2-} \tag{17}$$

$$S_2O_8^{2-} + M^{n+} \rightarrow {}^{\bullet}SO_4^- + SO_4^{2-} + M^{(n+1)+} \tag{18}$$

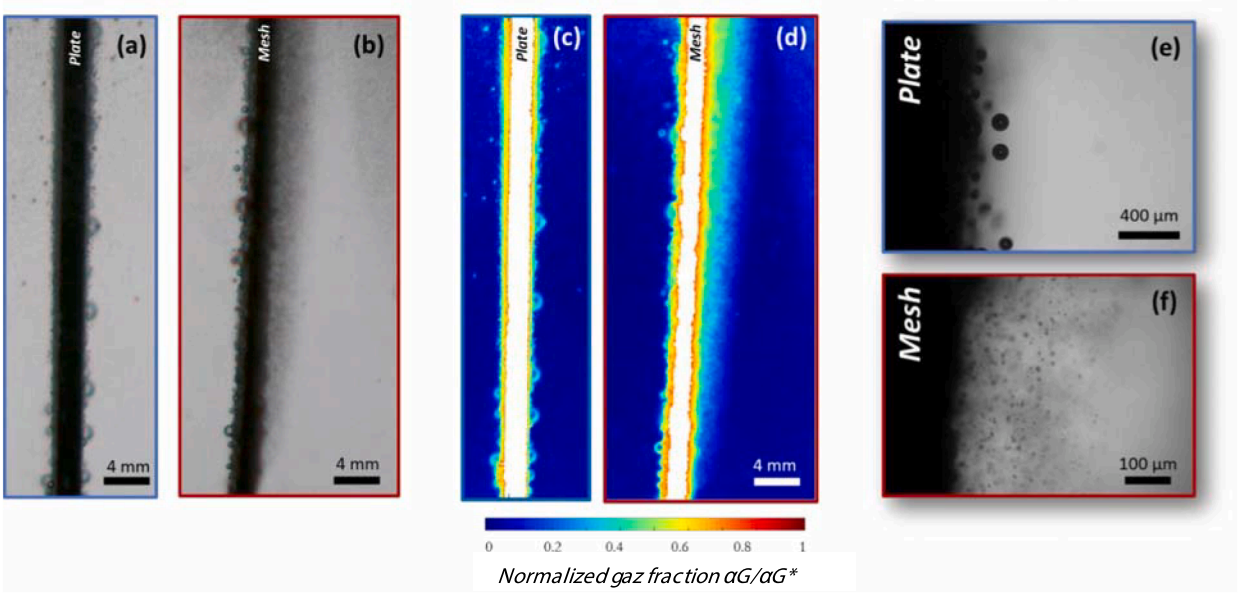

Fig. 9. Images, taken with macro lens, of a (a) plate and (b) mesh anode with (c) and (d) the respective color map image where red regions indicate higher gas fractions and yellow regions indicate lower ones, and images, taken with micro lens, of a (e) plate and (f) mesh anode in the following experimental conditions: Q_l = 10.8 L h^{-1}, $NaNO_3$ (50 mM) and I = 4 A. (For interpretation of the references to color in this figure legend, the reader is referred to the web version of this article.)

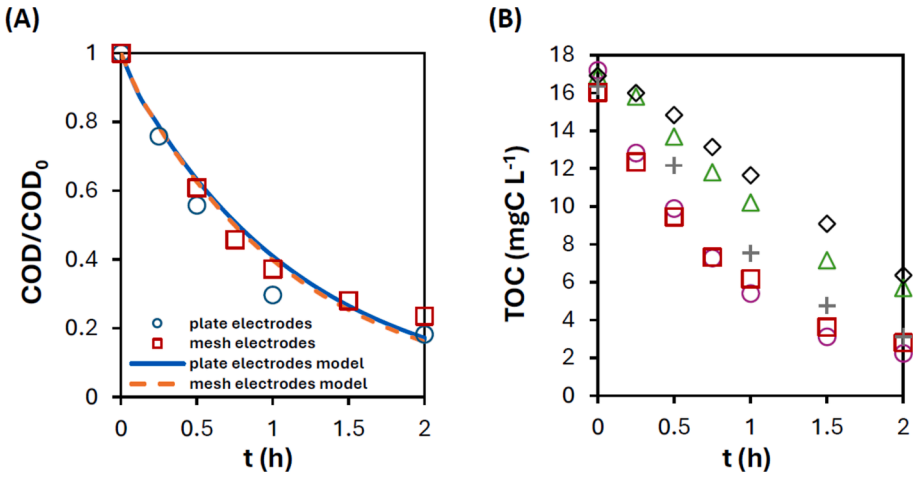

Fig. 10. (A) COD/COD_0 evolution versus phenol treatment time (h) at $V_T = 2.15$ L, $Q_l = 10.8$ L h^{-1}, $[COD]_0 = 50$ mgO_2 L^{-1} and $I = 4$ A for plate electrode configuration with Na_2SO_4 electrolyte (◯), mesh electrode configuration with Na_2SO_4 electrolyte (□) and the corresponding curves obtained from modeling for plate electrode (——) and mesh electrodes (— — —). (B) TOC (mgC L^{-1}) evolution versus time (h) at $V_T = 2.15$ L, $[COD]_0 = 40$ mgO_2 L^{-1} and $I = 4$ A for plate electrode configuration with $NaNO_3$ electrolyte at $Q_l = 10.8$ L h^{-1} (△)), plate electrode configuration with Na_2SO_4 electrolyte at $Q_l = 10.8$ L h^{-1} (◯), mesh electrode configuration with Na_2SO_4 electrolyte at $Q_l = 10.8$ L h^{-1} (□), mesh electrode configuration with $NaNO_3$ electrolyte at $Q_l = 10.8$ L h^{-1} (◇), and mesh electrode configuration with $NaNO_3$ electrolyte at $Q_l = 32.4$ L h^{-1} (+).

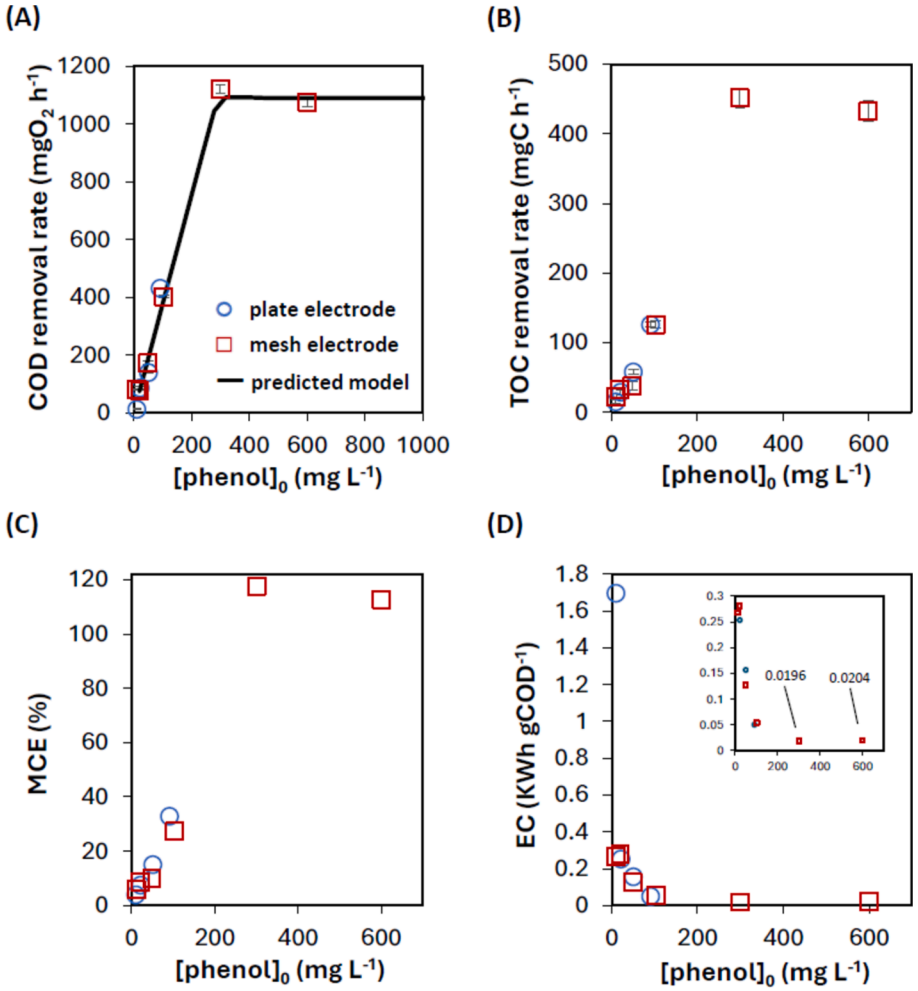

Fig. 11. (A) COD removal rate (mgO_2 h^{-1}) with predicted model (—), (B) TOC removal rate (mgC h^{-1}), (C) MCE (%), and (D) EC (KWh $gCOD^{-1}$) for different initial phenol concentrations (mg L^{-1}) with 50 mM Na_2SO_4, $Q_l = 10.8$ L h^{-1} and $I = 4$ A in single pass mode using plate electrode configuration (◯) and mesh electrode configuration (□).

Faster kinetics of TOC removal were obtained with Na_2SO_4 compared to $NaNO_3$ (Fig. 10b), thus highlighting the role of oxidation mediated by sulfate radicals in mineralization of phenol. In $NaNO_3$ electrolyte, the reaction zone cannot be extended to more than 1 μm from the electrode surface because of the short lifetime of hydroxyl radicals [13]. In Na_2SO_4 electrolyte, longer lifetime of sulfate radicals might involve an extension of the reaction zone. In this case, limitations related to mass transport of target compounds to the electrode surface might have a lower impact on process efficiency.

In Na_2SO_4 electrolyte, the calibrated value of k_m should be considered only as an apparent k_m ($k_{m,app}$) since the value comes from experimental results that do not only depend on mass transport of the target compound to the very near electrode surface. For the treatment of real effluent, the $k_{m,app}$ will therefore depend on the composition of the inorganic matrix. These $k_{m,app}$ values were evaluated with the same methodology than with $NaNO_3$ electrolyte. The same values were obtained for both configurations (0.83×10^{-3} cm s^{-1}) in the same operating conditions ($Q_l = 10.8$ L h^{-1} and $I = 4$ A). These results confirmed that mass transport conditions had a lower impact on process effectiveness (for mineralization of organic compounds) when the reaction zone is extended by mediated oxidation.

3.3.2. Operation of the reactor in single pass mode

Experiments were then performed in continuous mode (single pass through the reactor, 0 % recirculation) with Na_2SO_4 electrolyte for an initial concentration of phenol between 10 and 600 mg L^{-1}. The rates of COD and TOC removal are plotted in Fig. 11. Two different regimes appeared according to the value of the applied current density (j_{app}) compared to the limiting current density (j_{lim}, **Equation (2)**, calculated using values of $k_{m,app}$ presented in previous section) [14].

For low initial concentrations of phenol (10 – 100 mg L^{-1}), j_{app} was higher than j_{lim} and the process was operated under strong mass transport limitation. Thus, low COD and TOC removal rates were obtained. The MCE was low ranging 4 – 32 %, and the EC was high in term of kWh per g of COD removed ranging 1.7 – 0.05 (Fig. 11c and Fig. 11d). In fact, mass transport limitations promote waste reaction such as dimerization of $^{\bullet}OH$ (**Equation (19)**) instead of reactions with organic compounds [47].

$$^{\bullet}OH + {}^{\bullet}OH \rightarrow {}^{\bullet}H_2O_2 \quad (19)$$

In Ganiyu et al. (2016), a batch reactor setup with BDD anodes demonstrated a 60 % mineralization of a 19.6 mgC L^{-1} amoxicillin solution, achieving a mineralization current efficiency (MCE) of 15 % [48]. In contrast, our study, utilizing a continuous reactor, observed a 20 % mineralization of a 15 mgC L^{-1} phenol solution with an MCE of 8.6 % (Fig. 11). This comparison highlights the higher MCE obtained with the batch conditions, particularly due to vigorous stirring, which significantly enhances convective mass transport. This effect is challenging to replicate in large-scale continuous reactors. In our configuration, further improvement could be achieved by (i) increasing the flow rate or (ii) treating more concentrated effluents. Indeed, for higher initial concentrations of phenol (300 – 600 mg L^{-1}), j_{lim} increased and was higher than j_{app}. The treatment was operated under current limitation. COD and TOC removal rates reached a plateau around 1,100 mgO_2 h^{-1} (for COD) and 440 mgC h^{-1} (for TOC). In this case, values of MCE reached around 100 % and the EC decreased to 0.020 kWh $gCOD^{-1}$ (Fig. 11c and Fig. 11d). As observed in 100 % recirculation experiments (with Na_2SO_4 electrolyte), non-significant difference was obtained in term of COD and TOC removal between plate and mesh electrodes.

The advective – dispersive model with reaction was also used for predicting COD removal rates during single pass mode experiments. Previously calibrated values of $k_{m,app}$ and dispersion coefficient (D) were used. Comparison of model and experimental data highlighted a nearly perfect fit (Fig. 11a), with a predicted maximum removal rate reached starting from $[phenol]_0 = 300$ mg L^{-1} (i.e. when $j_{lim} = j_{app}$) in these operating conditions ($Q_l = 10.8$ L h^{-1} and $I = 4$ A).

Therefore, such model provides a versatile tool for sizing and operating this kind of reactor according to the intended application. As an illustration of the potential efficiency of the process for the treatment of a low concentration of pollutant, the model allows for predicting the reactor volume required to achieve 80 % COD removal in continuous mode (0 % recirculation) for a given set of operating conditions ($[COD]_0 = 50$ mgO_2 L^{-1}, $Q_l = 10.8$ L h^{-1} and $I = 4$ A, $D = 23.3$ mm^2 s^{-1} and $k_m = 0.83 \times 10^{-3}$ cm s^{-1}), corresponding to an energy consumption of 2.2 kWh m^{-3} when considering a cell potential of 5.5 V. In this case, the obtained value was $V_T = 14.8$ L. The corresponding surface area of electrodes was $S_T = 503$ cm^2, resulting in a space–time yield effectiveness of 8.7 g of DCO removed per m^2 of electrode and per hour. For comparison only 50 % COD removal would require a smaller reactor ($V_T = 6.4$ L) and less electrode surface ($S_T = 217$ cm^2), corresponding to a space–time yield of 12.4 of DCO removed per m^2 of electrode and per hour. Space-time yield effectiveness is limited in this case by current density and Faradaic efficiency (e.g. 36 % and 23 % in the case of the target of 80 and 50 % COD removal, respectively). Higher values would be obtained for the treatment of more concentrated effluents at higher current density. Employing a modular approach, where multiple modules operate in parallel, can offer a reliable solution for larger-scale applications. However, key factors in scaling up include (i) ensuring uniform current distribution across the electrodes, (ii) addressing electrode size limitations in terms of electrode manufacturing and (iii) identifying cost-effective materials with similar electrochemical properties.

3.3.3. Impact of D and k_m on process effectiveness

The impact of D and k_m on COD removal in single pass mode was then predicted using the advective – dispersive model with reaction (Fig. 12). Values of D and k_m were moved from −50 % to + 100 % based on values obtained in the experiment with mesh electrodes, Na_2SO_4 electrolyte, $Q_l = 10.8$ L h^{-1} and $I = 4$ A ($D = 23.3$ mm^2 s^{-1} and $k_m = 0.83 \times 10^{-3}$ cm s^{-1}). The results showed that doubling the value of the dispersion coefficient D, which describes a degree of turbulent mixing superimposed on the ideal plug flow, did not significantly affect COD removal (Fig. 12a). Besides, k_m value had a strong influence. Doubling the k_m value multiplied by 1.82 the mineralization yield of 50 mgO_2 L^{-1} (Fig. 12b). Increasing k_m would also allow for reaching the maximum COD removal rate (i.e. as observed in Fig. 11a) at lower initial concentration of pollutants. It is relevant with the operation of a process based on heterogeneous electrocatalysis under mass transport limitation. Overall, increasing k_m value appears as the key challenge for intensification of process effectiveness, as previously described in the literature. It might be obtained by (i) optimizing operating conditions (e.g., increase of liquid flow rate, as observed in Table 2), (ii) promoting the generation of oxidant species able to extend the reactive zone (as observed in Fig. 10), (iii) optimizing the morphology of mesh electrodes for improving convection near electrode surface and favoring detachment of gas bubbles.

4. Conclusions

Bubbles generated from OER and HER played a significant role in promoting micro-turbulences near the surface of electrodes, with a significant effect on hydrodynamics, particularly when it was operated at low liquid flow rate. Bubbles strongly reduced recirculation phenomena within the reactor. RTD curves obtained with current supply were similar to the behavior of the reactor with external aeration. Moreover, despite very different flow path, similar RTD curves were obtained when comparing configurations with plate and mesh electrodes under electric polarization, thus indicating that these micro-turbulences might be a major governing factor of RTD in such electrochemical reactor.

As regards to mass transport rate of target compounds to the electrode surface, micro-turbulence enhancement near the electrode surface

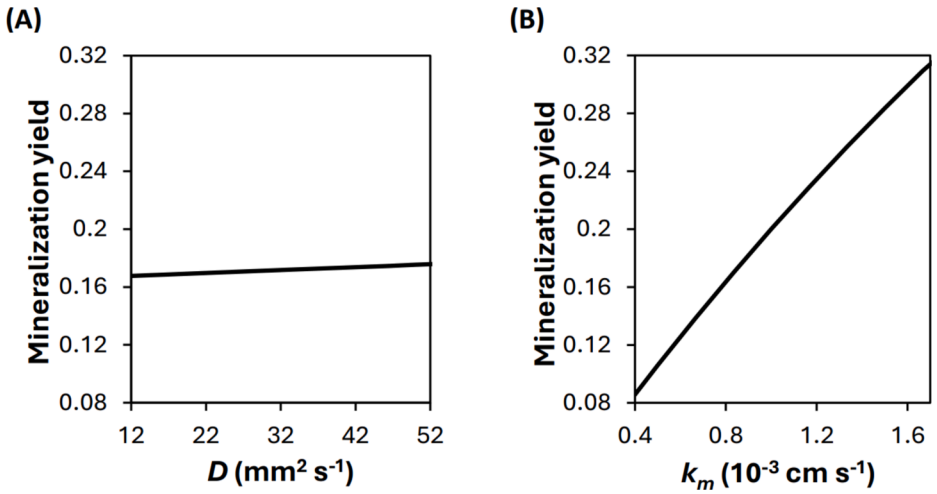

Fig. 12. Predicted mineralization yield ((COD_0-COD_f)/COD_0) in single pass mode *vs* (A) D (cm^2 min^{-1}) for a fixed k_m of 0.83 × 10^{-3} cm s^{-1} and (B) k_m (10^{-3} cm s^{-1}) for a fixed D of 23.3 mm^2 s^{-1} in the following operating conditions: $[COD]_0$ = 50 mgO_2 L^{-1}, Q_l = 10.8 L h^{-1} and I = 4 A.

as well as the decrease of the active electrode surface can impact mass transport rate at a different level depending on reactor configuration and operating conditions. When using low liquid flow rate in the configuration with plate electrodes, micro-turbulences associated to the formation of large bubbles might control liquid convection in the vicinity of the electrodes. On the opposite, when using high liquid flow rate and/or configuration with mesh electrodes, liquid flow rate and the related velocity profile might still be the main parameter. Moreover, detachment of smaller bubbles was observed when using mesh electrodes with a possible impact on the active electrode surface.

Besides, results obtained with different electrolytes showed that mediated oxidation by oxidant species with longer lifetime (e.g., sulfate radicals) might extend the reaction zone away from the electrode surface and increase the apparent mass transport coefficient, which appeared as the key parameter for intensification of process effectiveness.

Finally, the advective – dispersive model with reaction, combined to the methodology developed for accurate calibration of key model parameters allowed for prediction of process performances. Such approach is useful in view of sizing industrial application of such emerging process for wastewater treatment (according to the volume to be treated, concentration in the feed, target objective of COD removal, operating conditions).

CRediT authorship contribution statement

Màxim Gibert-Vilas: Writing – original draft, Methodology, Investigation, Formal analysis, Data curation. **Yoan Pechaud:** Writing – review & editing, Validation, Supervision, Project administration, Methodology, Funding acquisition, Conceptualization. **Abderrahmane Kherbeche:** Methodology, Investigation. **Nihal Oturan:** Supervision, Methodology. **Laurent Gautron:** Supervision. **Mehmet A. Oturan:** Writing – review & editing, Validation, Supervision. **Clément Trellu:** Writing – review & editing, Validation, Supervision, Project administration, Methodology, Funding acquisition, Conceptualization.

Declaration of competing interest

The authors declare that they have no known competing financial interests or personal relationships that could have appeared to influence the work reported in this paper.

Acknowledgments

Màxim Gibert-Vilas acknowledges Ministère français de l'Enseignement supérieur, de la Recherche et de l'Innovation for the financial support. All the authors also acknowledge I-SITE FUTURE for providing additional funding.

Appendix A. Supplementary data

Supplementary data to this article can be found online at https://doi.org/10.1016/j.cej.2024.157059.

Data availability

Data will be made available on request.

References

[1] R.K.B. Karlsson, A. Cornell, Selectivity between oxygen and chlorine evolution in the chlor-alkali and chlorate processes, Chem. Rev. 116 (2016) 2982–3028, https://doi.org/10.1021/acs.chemrev.5b00389.
[2] H. Shin, S. Lee, Y.-E. Sung, Industrial-scale H_2O_2 electrosynthesis in practical electrochemical cell systems, Curr. Opin. Electrochem. 38 (2023) 101224, https://doi.org/10.1016/j.coelec.2023.101224.
[3] D. Ewis, M. Arsalan, M. Khaled, D. Pant, M.M. Ba-Abbad, A. Amhamed, M.H. El-Naas, Electrochemical reduction of CO_2 into formate/formic acid: A review of cell design and operation, Sep. Purif. Technol. 316 (2023) 123811, https://doi.org/10.1016/j.seppur.2023.123811.
[4] J. Vehrenberg, J. Baessler, A. Decker, R. Keller, M. Wessling, Paired electrochemical synthesis of formate via oxidation of glycerol and reduction of CO_2 in a flow cell reactor, Electrochem. Commun. 151 (2023) 107497, https://doi.org/10.1016/j.elecom.2023.107497.
[5] Y. Liu, É. Lucas, I. Sullivan, X. Li, C. Xiang, Challenges and opportunities in continuous flow processes for electrochemically mediated carbon capture, iScience 25 (2022) 105153, https://doi.org/10.1016/j.isci.2022.105153.
[6] Z. Pan, Y. Liu, Z. Zhang, Z. Zhao, J. Zhu, R. Chen, L. An, A bifunctional electrochemical flow cell integrating ammonia production and electricity generation for renewable energy conversion and storage, Int. J. Hydrog. Energy 47 (2022) 38361–38371, https://doi.org/10.1016/j.ijhydene.2022.09.007.
[7] I. Sirés, E. Brillas, M.A. Oturan, M.A. Rodrigo, M. Panizza, Electrochemical advanced oxidation processes: today and tomorrow. A review, Environ. Sci. Pollut. Res. 21 (2014) 8336–8367, https://doi.org/10.1007/s11356-014-2783-1.
[8] C.A. Martinez-Huitle, M.A. Rodrigo, I. Sirés, O. Scialdone, Single and coupled electrochemical processes and reactors for the abatement of organic water pollutants: A critical review, Chem Rev (2015) 46, https://doi.org/10.1021/acs.chemrev.5b00361.
[9] N. Oturan, M.A. Oturan, Electro-Fenton process: background, new developments, and applications, in: Electrochem. Water Wastewater Treat, Elsevier, 2018, pp. 193–221, https://doi.org/10.1016/B978-0-12-813160-2.00008-0.
[10] C. Trellu, H. Olvera Vargas, E. Mousset, N. Oturan, M.A. Oturan, Electrochemical technologies for the treatment of pesticides, Curr. Opin. Electrochem. 26 (2021) 100677, https://doi.org/10.1016/j.coelec.2020.100677.

[11] S.A. Hien, C. Trellu, N. Oturan, A.S. Assémian, B.G.H. Briton, P. Drogui, K. Adouby, M.A. Oturan, Comparison of homogeneous and heterogeneous electrochemical advanced oxidation processes for treatment of textile industry wastewater, J. Hazard. Mater. 437 (2022) 129326, https://doi.org/10.1016/j.jhazmat.2022.129326.
[12] C.A. Martínez-Huitle, M.A. Rodrigo, I. Sirés, O. Scialdone, A critical review on latest innovations and future challenges of electrochemical technology for the abatement of organics in water, Appl. Catal. B Environ. 328 (2023) 122430, https://doi.org/10.1016/j.apcatb.2023.122430.
[13] A. Kapałka, G. Fóti, C. Comninellis, The importance of electrode material in environmental electrochemistry, Electrochimica Acta 54 (2009) 2018–2023, https://doi.org/10.1016/j.electacta.2008.06.045.
[14] M. Panizza, G. Cerisola, Direct and mediated anodic oxidation of organic pollutants, Chem. Rev. 109 (2009) 6541–6569, https://doi.org/10.1021/cr9001319.
[15] P.V. Nidheesh, G. Divyapriya, N. Oturan, C. Trellu, M.A. Oturan, Environmental applications of boron-doped diamond electrodes: 1. Applications in water and wastewater treatment, ChemElectroChem 6 (2019) 2124–2142, https://doi.org/10.1002/celc.201801876.
[16] L.R.D. Brito, S.O. Ganiyu, E.V. Dos Santos, M.A. Oturan, C.A. Martínez-Huitle, Removal of antibiotic rifampicin from aqueous media by advanced electrochemical oxidation: Role of electrode materials, electrolytes and real water matrices, Electrochim. Acta 396 (2021) 139254, https://doi.org/10.1016/j.electacta.2021.139254.
[17] A.A. Nada, B.O. Orimolade, H.H. El-Maghrabi, B.A. Koiki, M. Rivallin, M. F. Bekheet, R. Viter, D. Damberga, G. Lesage, I. Iatsunskyi, E. Coy, M. Cretin, O. A. Arotiba, M. Bechelany, Photoelectrocatalysis of paracetamol on Pd–ZnO/ N-doped carbon nanofibers electrode, Appl. Mater. Today 24 (2021) 101129, https://doi.org/10.1016/j.apmt.2021.101129.
[18] J. Ma, C. Trellu, N. Oturan, S. Raffy, M.A. Oturan, Development of Ti/TiOx foams for removal of organic pollutants from water: Influence of porous structure of Ti substrate, Appl. Catal. B Environ. 317 (2022) 121736, https://doi.org/10.1016/j.apcatb.2022.121736.
[19] J. Abidi, D. Clematis, Y. Samet, M. Delucchi, D. Cademartori, M. Panizza, Influence of anode material and chlorides in the new-gen solid polymer electrolyte cell for electrochemical oxidation – Optimization of Chloroxylenol degradation with response surface methodology, J. Electroanal. Chem. 920 (2022) 116584, https://doi.org/10.1016/j.jelechem.2022.116584.
[20] G. Ren, S. Lanzalaco, M. Zhou, P.L. Cabot, E. Brillas, I. Sirés, Replacing carbon cloth by nickel mesh as substrate for air-diffusion cathodes: H_2O_2 production and carbenicillin degradation by photoelectro-Fenton, Chem. Eng. J. 454 (2023) 140515, https://doi.org/10.1016/j.cej.2022.140515.
[21] Z. Wang, H. Olvera-Vargas, M.V. Surmani Martins, O. Garcia-Rodriguez, S. Garaj, O. Lefebvre, High performance and durable graphene-grafted cathode for electro-Fenton degradation of tetramethyldecynediol, Chem. Eng. J. 455 (2023) 140643, https://doi.org/10.1016/j.cej.2022.140643.
[22] D. Pletcher, F.C. Walsh, Industrial electrochemistry, 2nd edn., Chapman and Hall, London, 1990.
[23] F.C. Walsh, D. Pletcher, Electrochemical engineering and cell design, in: D. Pletcher, Z. Tian, D.E. Williams (Eds.), Dev. Electrochem., 1st ed., Wiley, 2014, pp. 95–111, https://doi.org/10.1002/9781118694404.ch6.
[24] F.C. Walsh, C.A.P. de Leon, Electrochemical cell design for water treatment, in: G. Kreysa, K. Ota, R.F. Savinell (Eds.), Encycl. Appl. Electrochem., Springer New York, New York, NY, 2014, pp. 462–464, https://doi.org/10.1007/978-1-4419-6996-5_134.
[25] Y. Ling, H. Xu, X. Chen, Continuous multi-cell electrochemical reactor for pollutant oxidation, Chem. Eng. Sci. 122 (2015) 630–636, https://doi.org/10.1016/j.ces.2014.10.031.
[26] J. Radjenovic, D.L. Sedlak, Challenges and opportunities for electrochemical processes as next-generation technologies for the treatment of contaminated water, Environ. Sci. Technol. 49 (2015) 11292–11302, https://doi.org/10.1021/acs.est.5b02414.
[27] I.M.S. Pillai, A.K. Gupta, Performance analysis of a continuous serpentine flow reactor for electrochemical oxidation of synthetic and real textile wastewater: Energy consumption, mass transfer coefficient and economic analysis, J. Environ. Manage. 193 (2017) 524–531, https://doi.org/10.1016/j.jenvman.2017.02.046.
[28] B.P. Chaplin, The Prospect of Electrochemical Technologies Advancing Worldwide Water Treatment, Acc. Chem. Res. 52 (2019) 596–604, https://doi.org/10.1021/acs.accounts.8b00611.
[29] H. Monteil, Y. Pechaud, N. Oturan, C. Trellu, M.A. Oturan, Pilot scale continuous reactor for water treatment by electrochemical advanced oxidation processes: Development of a new hydrodynamic/reactive combined model, Chem. Eng. J. 404 (2021) 127048, https://doi.org/10.1016/j.cej.2020.127048.
[30] J. Hereijgers, J. Schalck, T. Breugelmans, Mass transfer and hydrodynamic characterization of structured 3D electrodes for electrochemistry, Chem. Eng. J. 384 (2020) 123283, https://doi.org/10.1016/j.cej.2019.123283.
[31] F.F. Rivera, C.P. De León, J.L. Nava, F.C. Walsh, The filter-press FM01-LC laboratory flow reactor and its applications, Electrochimica Acta 163 (2015) 338–354, https://doi.org/10.1016/j.electacta.2015.02.179.
[32] F.F. Rivera, C.P.D. León, F.C. Walsh, J.L. Nava, The reaction environment in a filter-press laboratory reactor: the FM01-LC flow cell, Electrochimica Acta 161 (2015) 436–452, https://doi.org/10.1016/j.electacta.2015.02.161.
[33] F.C. Walsh, C. Ponce de León, Progress in electrochemical flow reactors for laboratory and pilot scale processing, Electrochimica Acta 280 (2018) 121–148, https://doi.org/10.1016/j.electacta.2018.05.027.
[34] F.C. Walsh, L.F. Arenas, C. Ponce De León, Developments in plane parallel flow channel cells, Curr. Opin. Electrochem. 16 (2019) 10–18, https://doi.org/10.1016/j.coelec.2019.02.006.
[35] L.F. Arenas, C. Ponce De León, F.C. Walsh, Critical Review—The Versatile Plane Parallel Electrode Geometry: An Illustrated Review, J. Electrochem. Soc. 167 (2020) 023504, https://doi.org/10.1149/1945-7111/ab64ba.
[36] F.H. Adnan, M.-N. Pons, E. Mousset, Mass transport evolution in microfluidic thin film electrochemical reactors: New correlations from millimetric to submillimetric interelectrode distances, Electrochem. Commun. 130 (2021) 107097, https://doi.org/10.1016/j.elecom.2021.107097.
[37] F.C. Walsh, L.F. Arenas, C. Ponce De León, Editors' Choice—Critical Review—The Bipolar Trickle Tower Reactor: Concept, Development and Applications, J. Electrochem. Soc. 168 (2021) 023503, https://doi.org/10.1149/1945-7111/abdd7a.
[38] L. Guo, Y. Jing, B.P. Chaplin, Development and Characterization of Ultrafiltration TiO_2 Magnéli Phase Reactive Electrochemical Membranes, Environ. Sci. Technol. 50 (2016) 1428–1436, https://doi.org/10.1021/acs.est.5b04366.
[39] C. Trellu, B.P. Chaplin, C. Coetsier, R. Esmilaire, S. Cerneaux, C. Causserand, M. Cretin, Electro-oxidation of organic pollutants by reactive electrochemical membranes, Chemosphere 208 (2018) 159–175, https://doi.org/10.1016/j.chemosphere.2018.05.026.
[40] K. Groenen Serrano, A critical review on the electrochemical production and use of peroxo-compounds, Curr. Opin. Electrochem. 27 (2021) 100679, https://doi.org/10.1016/j.coelec.2020.100679.
[41] F. Ghanbari, M. Moradi, Application of peroxymonosulfate and its activation methods for degradation of environmental organic pollutants: Review, Chem. Eng. J. 310 (2017) 41–62, https://doi.org/10.1016/j.cej.2016.10.064.
[42] P. Cañizares, J. García-Gómez, I. Fernández de Marcos, M.A. Rodrigo, J. Lobato, Measurement of Mass-Transfer Coefficients by an Electrochemical Technique, J. Chem. Educ. 83 (2006) 1204, https://doi.org/10.1021/ed083p1204.
[43] J. Winkelmann, Diffusion in Gases, Liquids and Electrolytes: Nonelectrolyte Liquids and Liquid Mixtures - Part 2: Liquid Mixtures, Springer, Berlin Heidelberg, Berlin, Heidelberg, 2018, 10.1007/978-3-662-54089-3.
[44] S. Abdelghani-Idrissi, N. Dubouis, A. Grimaud, P. Stevens, G. Toussaint, A. Colin, Effect of electrolyte flow on a gas evolution electrode, Sci. Rep. 11 (2021) 4677, https://doi.org/10.1038/s41598-021-84084-1.
[45] S. Li, Y. Yang, H. Zheng, Y. Zheng, T. Jing, J. Ma, J. Nan, Y.K. Leong, J.-S. Chang, Advanced oxidation process based on hydroxyl and sulfate radicals to degrade refractory organic pollutants in landfill leachate, Chemosphere 297 (2022) 134214, https://doi.org/10.1016/j.chemosphere.2022.134214.
[46] X. Duan, X. Niu, J. Gao, S. Wacławek, L. Tang, D.D. Dionysiou, Comparison of sulfate radical with other reactive species, Curr. Opin. Chem. Eng. 38 (2022) 100867, https://doi.org/10.1016/j.coche.2022.100867.
[47] E. Brillas, I. Sirés, M.A. Oturan, Electro-Fenton process and related electrochemical technologies based on Fenton's reaction chemistry, Chem. Rev. 109 (2009) 6570–6631, https://doi.org/10.1021/cr900136g.
[48] S.O. Ganiyu, N. Oturan, S. Raffy, M. Cretin, R. Esmilaire, E. Van Hullebusch, G. Esposito, M.A. Oturan, Sub-stoichiometric titanium oxide (Ti_4O_7) as a suitable ceramic anode for electrooxidation of organic pollutants: A case study of kinetics, mineralization and toxicity assessment of amoxicillin, Water Res. 106 (2016) 171–182, https://doi.org/10.1016/j.watres.2016.09.056.